Analysis of 38 GHz mmWave Propagation Characteristics of Urban Scenarios

Rodriguez Larrad, Ignacio; Nguyen, Huan Cong; Sørensen, Troels Bundgaard; Elling, Jan; Holm, Jens Åge; Mogensen, Preben; Vejlgaard, Benny

Published in:
European Wireless 2015; 21th European Wireless Conference; Proceedings of

Publication date:
2015

Document Version
Accepted author manuscript, peer reviewed version

Analysis of 38 GHz mmWave Propagation Characteristics of Urban Scenarios

Ignacio Rodriguez[1], Huan C. Nguyen[1], Troels B. Sørensen[1], Jan Elling[2], Jens Åge Holm[2], Preben Mogensen[1,3] and Benny Vejlgaard[3]

[1]Department of Electronic Systems, Aalborg University, Denmark, {irl, hcn, tbs, pm}@es.aau.dk
[2]Telenor A/S, Aalborg, Denmark, {jae, jeh}@telenor.dk
[3]Nokia Networks, Research Center Aalborg, Denmark, {preben.mogensen, benny.vejlgaard}@nsn.com

***Abstract*—The 38 GHz mm-wave frequency band is a strong candidate for the future deployment of wireless systems. Compared to lower frequency bands, propagation in the 38 GHz band is relatively unexplored for access networks in urban scenarios. This paper presents a detailed measurement-based analysis of urban outdoor and outdoor-to-indoor propagation characteristics at 38 GHz. Different sets of measurements were performed in order to understand, quantify and model the behavior of the different underlying propagation mechanisms. The study considers line-of-sight propagation, reflection, scattering, diffraction, transmission, as well as polarization effects. The measurement results confirm that, at this particular frequency, propagation in urban scenarios is mainly driven by line-of-sight and reflection. The proposed models are practical for implementation in system level simulators or ray-tracing tools. The different observations presented along the paper are useful for future radio network planning considerations.**

***Keywords*—mmWave Communications, 38 GHz, Urban Radio Propagation, LOS, NLOS, Reflection, Scattering, Diffraction, Transmission, Polarization.**

I. Introduction

An increase of 10,000 times in mobile data traffic has been forecasted by 2020 [1]. This is expected not only due to the increase in the number of broadband users, but also due to the higher utilization of mobile services. Future wireless networks need to handle this traffic increase while, at the same time, they must improve the user experience by offering much higher data rates and much lower latency than what is offered nowadays. In order to cope with these demands, two approaches can be taken. The first one is the evolution of the 4G systems (LTE and LTE-A) through different strategies such as macro cell densification, small cell deployment, interference rejection/coordination techniques or MIMO enhancements. As an alternative, the design of a new 5G multi-RAT (radio access technology) local area system has attracted the focus in the last few years [1]. Some of the main drivers for this system are: simplicity, low cost design, low power, energy efficiency, self-optimization of ultra dense deployments, and also flexibility in spectrum usage. Whichever approach is taken, utilization of non-traditional cellular spectrum for wireless broadband access is inevitable, including cm-wave bands (e.g. 10 and 20 GHz) and mm-wave bands (30-300 GHz) with large contiguous bandwidth opportunities [2, 3], since below 6 GHz the scarce spectrum available is a very limiting factor and cannot meet the demands of future networks.

One of the potential mm-wave candidates is the 38 GHz frequency band, with approximately 4 GHz of available bandwidth. This band has been typically used only for line-of-sight (LOS) point-to-point links with high power and very directive antennas [4, 5]. The concept of local multipoint distribution system (LMDS) for carrier frequencies in the 20 to 40 GHz range exists since 1994 [6]. However, it was not until nowadays, that recent propagation studies have shown the real potential of this band to be used for point-to-multipoint access in dense outdoor urban scenarios. In [7], the authors reported some statistics of the multipath and time varying channel behaviors of short-hop millimeter-wave point-to-multipoint radio links in different urban scenarios. The measurement-based study in [8] showed the viability of cells with up to 200 m radius with very low outage by using reasonable power levels and directional antennas. Reference [2] compiles the results from different measurement campaigns and presents models for building penetration loss and urban propagation at 28 GHz, and suburban propagation at 38 GHz. In addition to this, the authors in [9], performed a coverage simulation of a 5G network based on the previous models and concluded that, compared to current 4G, a 2-3 times denser network topology will be necessary.

All the previous measurement-based studies consider realistic base station locations in elevated positions, and report results from measurements performed at random locations with the aim of collecting statistics on different propagation parameters such as path loss exponents, number of multipath components, delay spread or angles of arrival. With this information, it is possible to understand the real coverage potential of the cells operating at this frequency band, as well as performing system level simulations based on the simple propagation models. An interesting result in [10] was that, for 38 and 60 GHz, many unique paths can be formed in NLOS (non-line-of-sight) and LOS channels using narrow beam antennas. However, from these measurements, it was not possible to fully identify or model the dominant propagation mechanisms.

This paper complements the previous work by addressing the propagation in urban scenarios through a set of controlled measurements performed with ultra-narrow beam antennas located close to street level. With this particular setup, it is possible to perform high-resolution measurements, which allows to fill in the gaps from previous studies, and identify, model and compare each of the individual contributions of the different propagation mechanisms to the complex end-to-end propagation. The study considers LOS propagation, reflection, scattering, diffraction, transmission, along with polarization effects. In order to resemble the urban propagation environment, street canyon and corner scenarios are considered, as well as an outdoor-to-indoor scenario. The proposed models will be mainly applicable in ray-tracing predictions or system level simulations performed over scenarios with similar characteristics (e.g. building composition) to the ones presented in this paper. However, the general findings and indications about dominant propagation mechanisms will remain when addressing other urban scenarios with different characteristics.

The rest of the paper is organized as follows: Section II describes the different aspects of the measurement campaign such as the setup used, the scenarios considered, as well as the calibration and measurement procedures. Section III presents the results and the discussion and, finally, Section IV concludes the paper.

II. Measurement Campaign

A. Measurement Setup

In order to perform the measurements, commercial 38 GHz backhaul equipment was installed at both transmitter (TX) and receiver (RX) sides of the setup. An overview of the whole measurement system is depicted in Fig. 1. Modems and radio access units (RAU) for signal generation, transmission and reception were installed. As it can be seen in Fig. 2, both antennas were the same type and were installed at 1.75 m height on their respective locations. The TX antenna was mounted on a manual-operated trolley, meanwhile the RX antenna was mounted on a rotating pedestal externally controlled and steered in both azimuth and elevation. The radiation pattern of the antennas was highly directional (pencil-beam shaped) with a half power beamwidth (HPBW) of 1.5 degrees and a maximum gain of 40.5 dBi and 39 dBi for vertical (V) and horizontal (H) polarizations, respectively.

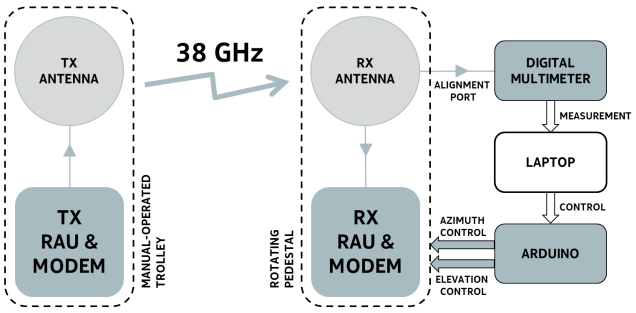

Fig. 1. Overview of the measurement system.

Fig. 2. Overview of antenna mountings at 1.75 m height on the manual-operated trolley (TX) and rotating pedestal (RX).

B. Calibration and Measurement Procedures

In order to perform the measurements, a multimeter was connected to the antenna alignment port of the RX RAU. Since the voltage at the antenna alignment port was proportional to the received power reported in the RX modem, performing voltage measurements allowed to speed up the measurement procedure. In post-processing, the voltage (V) readings were translated into received power (P_{rx}) samples by applying the simple relationship defined below in (1).

$$P_{rx}[\text{dBm}] = -\left(120 - \left(|V|/40\right)\right) \quad (1)$$

These post-processed power values are representative of the total RF power within the 28 MHz channel bandwidth. In order to validate this measurement procedure, a calibration was performed by comparing the post-processed power samples with the values reported at the RX modem. A maximum difference of 0.5 dB was found over a total of 45 readings.

The total output power at the TX was set to a fixed value of -10 dBm, in order to not saturate the RX at close LOS distances. Since the maximum sensitivity of the RX was -20 dBm, by considering the maximum antenna gain value and free space propagation, the minimum measurable distance was estimated to be approximately 25 m in LOS conditions. The minimum signal strength detectable was -95 dBm, resulting in a dynamic range of 75 dB.

Due to the narrow-beam antenna patterns, performing reliable controlled measurements with these type of antennas can only be achieved with a perfect alignment between maximums of the TX and RX antenna radiation patterns. Before every measurement, an initial alignment procedure was carried out as illustrated in Fig. 3.

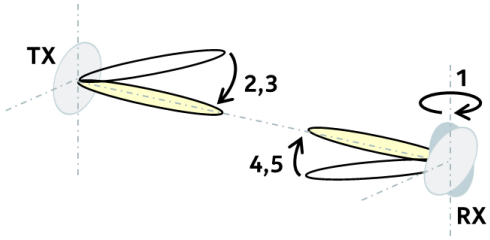

Fig. 3. Overview of the initial antenna alignment procedure.

The alignment was done separately for TX and RX, as well as for azimuth and elevation, by maximizing the received power (multimeter reading) in each of the following steps:

1) Orient RX antenna towards the expected angle of arrival (does not need to be very accurate).
2) Rotate TX antenna until finding maximum in azimuth.
3) Adjust TX antenna tilt until finding maximum in elevation.
4) Repeat 2) for the RX antenna.
5) Repeat 3) for the RX antenna.

After this procedure, the measurement was performed by scanning different directions of arrival around the initial aligned position. The RX antenna was rotated by the pedestal in azimuth and elevation, exploring a grid of 8x10 degrees. The received power was obtained for each of the points of the grid and, finally, the maximum value was selected as an outcome of the measurement. As it can be deduced from the measurement example presented in Fig. 4, an incorrect sampling (i.e. outside the HPBW) could rapidly result in large deviations (up to 30 dB) from the maximum value. The resolution of the rotating pedestal was set to 0.5 degrees. With this value, smaller than half of the HPBW, it is ensured that at least one of the scanned positions during the measurement matched inside the HPBW antenna radiation patterns at both TX and RX. This makes the overall measurement procedure to be more robust to potential small errors committed during the antenna alignment stage.

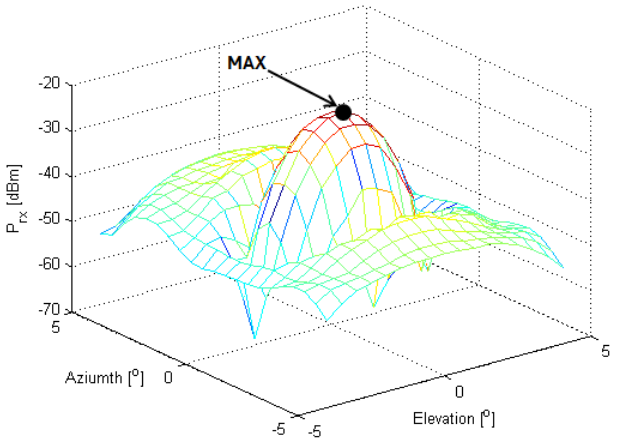

Fig. 4. LOS measurement example with 30 m distance between TX and RX.

The total procedure including setup, alignment and (scanning) measurement was very time consuming. Every individual sample presented in the following section of results required at least 30-40 min to be obtained, meanwhile the data presented in the polar plots took even longer (45-90 min) due to the half/full azimuth range scanned with the aforementioned resolution. On the other hand, these long measurement procedures allowed us to work on a ray-based level, making possible to isolate and quantify the contributions from the different propagation phenomena of interest with great accuracy.

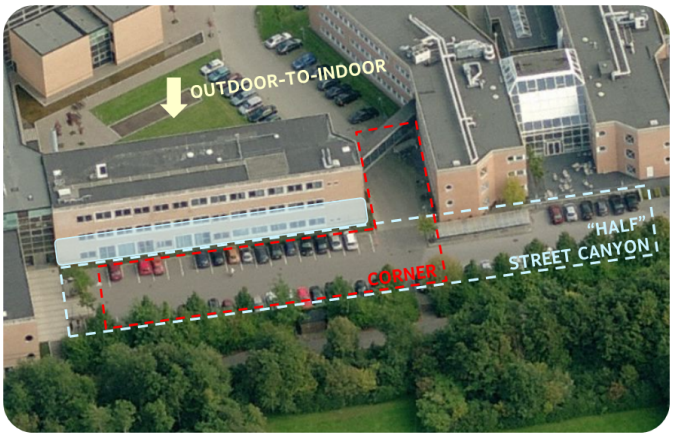

Fig. 5. Aerial view of the measurement area at the Department of Electronic Systems of Aalborg University, Denmark [Bing Maps, © Nokia, MS 2014].

C. Measurement Scenarios

The measurement campaign was performed at one of the parking areas of the Department of Electronics Systems at Aalborg University, Denmark (Fig. 5). During the measurements, the parking lot was closed and empty of cars in order to ensure the most static channel conditions possible during the controlled experiments. This is a large flat area which allowed to reproduce three measurement scenarios representative of the urban radio propagation:

1) Outdoor "half" street canyon scenario: large open space in the front part of the measurement area. In this scenario, LOS propagation up to a maximum distance of approximately 90 m was investigated, as well as reflection and scattering on the 3-storey building parallel to the parking area (shadowed on the illustration in Fig. 5).
2) Outdoor corner scenario: area formed by the front parking lot area and the perpendicular street canyon. This scenario was used to analyze propagation around corners by addressing different diffraction situations.
3) Outdoor-to-indoor scenario: with the aim of characterizing transmission, different sets of penetration loss measurements were performed in the yard, at the back-side part of the aforementioned building, following a similar procedure to our previous study [11].

The geometry considered in each of the scenarios for planning and, subsequently, analyzing the measurements for the different propagation mechanisms is presented in Fig. 6.

III. Results and Discussion

A. Line-of-Sight (LOS)

A number of measurements was performed at different distances between TX and RX for the diverse polarization configurations[1]: VVpol (both the TX and the RX antennas were vertically polarized), HHpol (both the TX and the RX antennas were horizontally polarized, respectively), and VHpol (the TX antenna was vertically polarized, meanwhile the RX antenna was horizontally polarized).

[1]For this particular set of equipment, the desired polarization can be set directly inside of the RAU without any physical change on the setup (e.g. same antenna position and orientation).

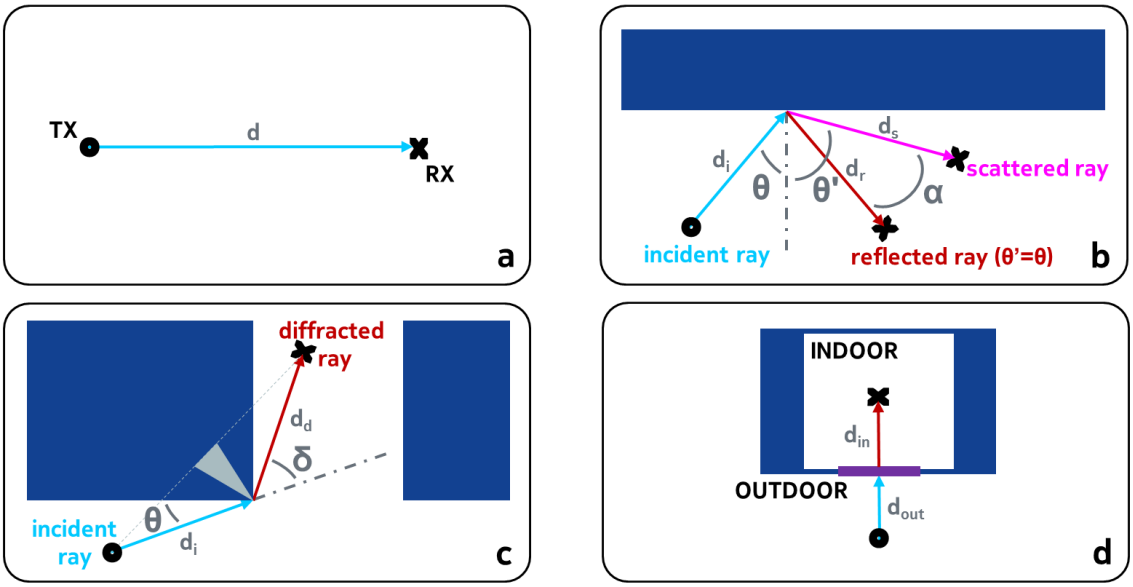

Fig. 6. Detailed geometry of the different measurement scenarios considered for each of the individual propagation mechanisms: a) LOS, b) reflection and scattering, c) diffraction, d) transmission.

Path loss (PL) was estimated from the different LOS power samples measured ($P_{rx,LOS}$) at different distances (d), by applying (2) according to the geometry in Fig. 6.a. The corresponding TX and RX antenna gain values (G_{tx}, G_{rx}) were considered in accordingly to the selected polarization configuration. These values were already reported in Section II, as well as the transmit power (P_{tx}). In the case of VHpol, the extra term L_{pol} was included in order to account for the loss due to polarization mismatch. This loss factor was found to be 16.75 dB, on average, based on all the different VHpol measurements performed along the campaign[2].

$$PL(d)[\text{dB}] = P_{tx} - P_{rx,LOS}(d) + G_{tx} + G_{rx} - L_{pol} \qquad (2)$$

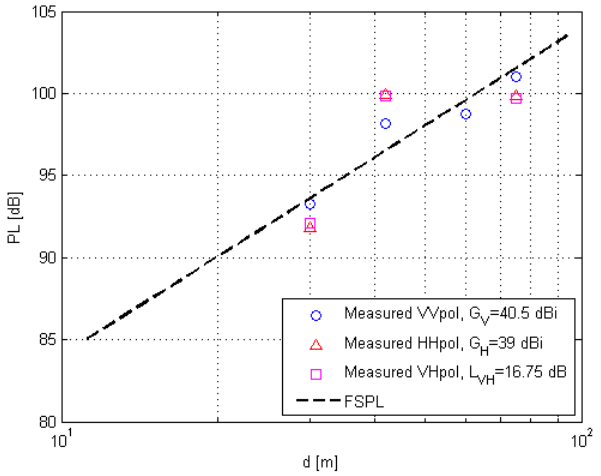

Fig. 7. Path loss in LOS conditions for the different polarization configurations, and comparison with FSPL.

[2]VHpol measurements are only presented for LOS. However, they were also performed for all the different situations considered in the study, finding a very similar offset with respect to VVpol and HHpol in all the cases.

Fig. 7 presents the resultant path loss samples for the different TX-RX distances considered. As it can be seen, under LOS conditions, propagation follows free space (FS) independently of the polarization configuration selected, with a maximum absolute deviation of 3.2 dB. This was an expected result, similar to our previous experiences reported in [12] for lower frequency bands, and provides further validation to the calibration, alignment and measurement procedures.

B. *Reflection and Scattering*

In urban scenarios, radio signals propagate along the streets canyons driven mainly by LOS propagation, but also by reflection and scattering over the surrounding buildings. In order to analyze these last two mechanisms, measurements were performed according to the disposition displayed in Fig. 6.b, where both the TX and RX antennas were pointed towards the facade of the building of interest, in order to explore different angular configurations.

First, (specular) reflection was addressed. In this case, the incident angle (θ) and the reflected angle (θ') are equal with respect to the normal plane of incidence over the building ($\theta = \theta'$). Measurements were done for a number of different incident/reflected angles for both VVpol and HHpol configurations. In order to characterize this mechanism, reflection loss (L_r) is defined as indicated in (3) as the difference between the LOS power, predicted according to the model in (2), at a distance equal to the total path length traveled by the ray ($d_i + d_r$) and the received power measured at that particular distance and reflected angle ($P_{rx,r}$). This allows to remove the distance dependence and isolate the angular behavior of the reflection mechanism.

$$L_r(\theta')[\text{dB}] = P_{rx,LOS}(d_i + d_r) - P_{rx,r}(d_i + d_r, \theta') \qquad (3)$$

The resultant reflection loss samples are shown in Fig. 8 for the different angles explored.

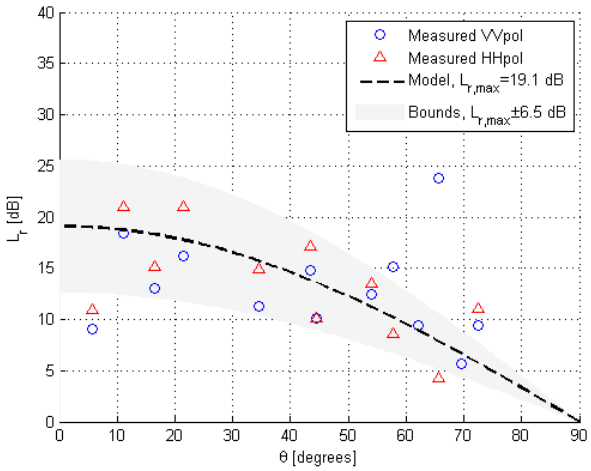

Fig. 8. Reflection loss with respect to the incident/reflected angle for the different polarization configurations.

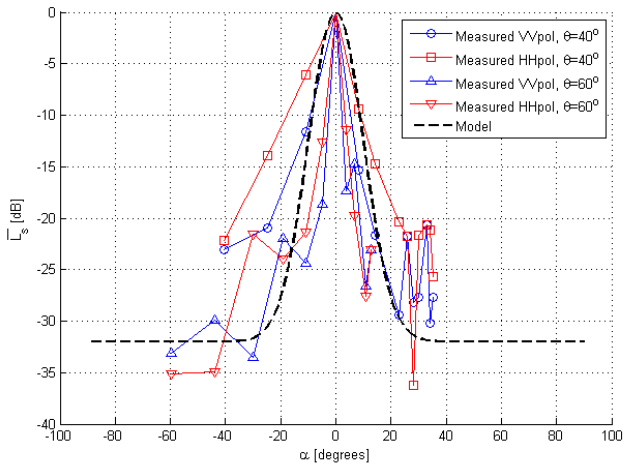

Fig. 9. Normalized scattering loss with respect to the angular difference between the main central reflected component and the scattered component for the different polarization configurations.

As it is shown, reflection loss decreases with increasing incident angle. In other words, the reflected components are stronger for larger incident angles. It can also be seen that both HHpol and VVpol present a very similar behavior, which. on average, can be approximated by the expression in (4), by simply considering a maximum reflection loss value ($L_{r,max}$). This value for the model is estimated according to (5) as the average value of the measurement data after compensating for the angular dependence.

$$L_r(\theta')[\text{dB}] = L_{r,max} \cdot cos(\theta) \tag{4}$$

$$L_{r,max}[\text{dB}] = \frac{1}{N}\sum_{i=1}^{N}\frac{L_r(\theta_i')}{cos(\theta_i')} = 19.1 \text{ dB} \tag{5}$$

The shaded area in Fig. 8 represents one standard deviation (68% of the samples for an approximate Gaussian distribution), considering the proposed model in (4) and the standard deviation of the $L_{r,max}$ estimate after removing the "outliers" in the data. Only one sample, with increased attenuation for VVpol at around 65 degrees of incidence angle, was removed. This sample would indicate the existence of a Brewster angle for vertical polarization, as predicted by standard Fresnel theory [13] and in line with existing observations previously reported in the literature [14].

Clearly, the simple empirical model proposed in (4) does not account for Brewster angle. However, it still follows the general behavior defined in the standard Fresnel theory [13]. By applying the selected maximum reflection value of 19.1 dB, the model fits the measurement data with a root mean square error (RMSE) of 4.9 dB. The deviation of the measurement data can be explained from the change of illuminated facade area for each different incident angle and from the mixed composition of the facade of the building (bricks, concrete, energy-efficient windows, aluminum frames ...). At this frequency, there are elements with a size comparable to a wavelength, which makes the facade to appear as a rough surface of reflection. As it was previously pointed out for lower frequencies in [15], this fact makes it difficult to predict the reflection behavior based on the theoretical Fresnel models, which assume incidence over infinite homogeneous dielectric planes and, therefore, empirical models as the one presented in this paper are needed.

In the case of non-specular or diffuse reflection (scattering), as indicated in Fig. 6.b, the reflected (scattered) angle (θ') is different to the incident angle ($\theta' \neq \theta$). Measurements were performed for two different incident angles (40 and 60 degrees), and a wide range of scattered angles, for both VVpol and HHpol polarization configurations.

Scattering loss (L_s) is defined in (6) as the difference between the LOS power at a distance equal to the total path length traveled by the ray ($d_i + d_s$) and the received power measured at that particular distance and scattered angle ($P_{rx,s}$). In order to remove the dependence on the incident angle, a normalized scattering loss ($\overline{L_s}$) is defined in (7) as the difference between the scattering loss at a particular scattered angle and the reflection loss at the correspondent incident/reflected angle. By doing this, scattering loss is characterized based on the angular difference between the different scattered components with respect to the main reflected component ($\alpha = \theta' - \theta$).

$$L_s(\theta')[\text{dB}] = P_{rx,LOS}(d_i + d_s) - P_{rx,s}(d_i + d_s, \theta') \tag{6}$$

$$\overline{L_s}(\alpha)[\text{dB}] = L_r(\theta) - L_s(\theta') \tag{7}$$

Fig. 9 presents the normalized scattering loss samples obtained from the measurements at the two different incident angles for the polarization configurations considered. As it can be seen, the results confirm that the scattered components spread around the main reflected component ($\alpha = 0$) with attenuated amplitude for increased angular difference between the diffuse and the central specular components. An interesting aspect observed from the figure is that, for absolute angular differences larger than 30 degrees, the scattering loss becomes quite constant in terms of amplitude. This fact suggests that, above this angular difference, the direct scattered components are not that strong and begin to be dominated by other components arriving from different angles.

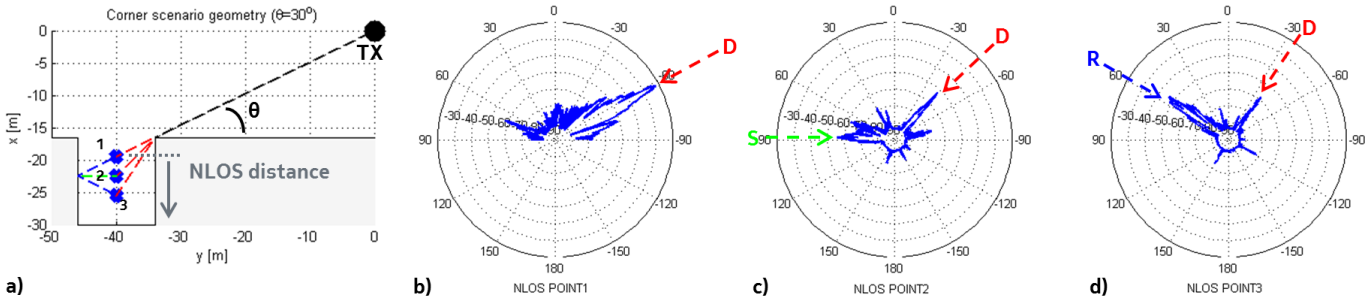

Fig. 10. a) Geometry of the three different measurement positions considered in the NLOS corner scenario for an incident angle of 30 degrees. b) Azimuthal power measured in dBm at point 1, c) Azimuthal power measured in dBm at point 2, d) Azimuthal power measured in dBm at point 3.

The behavior is very similar for both polarizations and, despite that there are some differences between the data from the two incident angles examined, a single model is considered for simplicity. As defined in (8), this model characterizes the normalized scattering loss as a Gaussian function with an amplitude of -32 dB and a standard deviation of 10 dB.

$$\overline{L_s}(\alpha)[\text{dB}] = -32 \cdot \left(1 - exp\left(\frac{-\alpha^2}{2 \cdot 10^2}\right)\right) \quad (8)$$

Considering this model, the RMSE to the measurements is 5.6 dB, very similar to the one previously presented for reflection loss. This can be explained, once again, from the different illuminated areas and the roughness of the reflection surface, which causes dispersion of the measurement data.

The results for reflection and scattering over the building presented in this section, can be compared to the results from [16]. In that particular study, the specular reflection loss for an incident angle of 30 degrees was found to be 13.7 dB (2.8 dB lower than in our case). About the normalized scattered components, they reported a spread of approximately ± 15 degrees around the main reflected component, reaching to a minimum level of approximately -20 to -25 dB. The different results from both studies can be easily explained from a different building structure or material composition.

C. Diffraction

The urban outdoor propagation analysis was completed by addressing the corner scenario, aimed to study propagation in pure NLOS conditions. In this respect, the TX antenna was pointed to the corner of the building and measurements were performed at different obstructed RX positions inside the street canyon, as indicated in Fig. 6.c. Two different incident angles (30 and 43 degrees) and three NLOS positions were considered for the different VVpol and HHpol configurations. In this case, the azimuthal range scanned was either 180 or 360 degrees (much larger than in the previous cases) in order to identify, quantify and compare all the potential contributions from the different propagation mechanisms to NLOS propagation. In this sense, the analysis focused not only on the previously studied mechanisms (reflection and scattering) but also on diffraction. Fig. 10.a illustrates the geometry of the scenario considering the different RX measurement positions. The first position considered was the middle point of the street canyon at which the TX antenna beam was half-shadowed by the corner at each considered incident angle. The second and third RX positions examined were also points in the middle of the street but with increased NLOS distance inside the canyon (3 and 6 m, respectively). This ensures three samples for different diffraction angles with respect to the corner, as well as increasing NLOS distances into the street canyon.

Fig. 10.b, Fig. 10.c and Fig. 10.d show the results of the 180 or 360 degrees scans at the three different positions with a considered incident angle (θ) of 30 degrees. The angular geometry can be easily related to the illustration in Fig. 10.a., facilitating a better understanding of the different propagation situations at each position. As it can be seen, at the first point, the major contribution was a diffracted component (red, D) arrived directly from the corner. The amplitude of this component was -31 dBm, exactly 6 dB lower than the power for a non-obstructed LOS link of the same length (44.5 m) calculated according to (2). This fact confirms the potential of applying the theoretical knife-edge diffraction model [17] also in this frequency band. At the second point, it can be observed how the major contribution was, again, the corner-diffracted component (-58 dBm). However, it can also be seen how the scattering component (green, S) in the region around 90 degrees is comparable in strength (-55 dBm). Finally, at the third position, it is noticeable how the reflected component (blue, R) was clearly stronger than the diffracted component (-54 and -71 dBm, respectively). At both the second and the third points, other scattered components coming from different indirect paths were below -80 dBm.

The measurement results confirm that, at this frequency, diffracted components exist but attenuate rapidly with increasing NLOS distances and, therefore, urban NLOS scenarios at this frequency are reflection-driven. This fact was already suggested in [8] and [10], however the authors could not verify it due to the lack of resolution with their measurement system.

In order to characterize the diffraction mechanism based on the different measurements, diffraction loss (L_d) is defined in (9) as the difference between the LOS power at a distance equal to the total path length traveled by the ray ($d_i + d_d$) and the diffracted power ($P_{rx,d}$) measured at that particular distance and interaction angle (δ).

$$L_d(\delta)[\text{dB}] = P_{rx,LOS}(d_i + d_d) - P_{rx,d}(d_i + d_d, \delta) \quad (9)$$

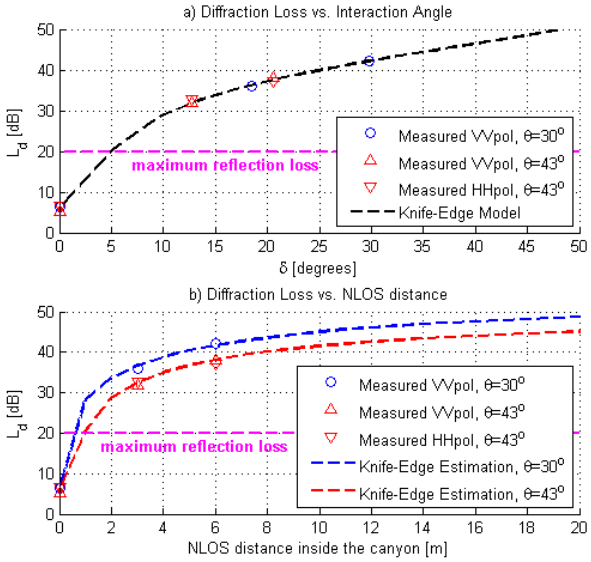

Fig. 11. Diffraction loss for the different polarization configurations with respect to: a) interaction angle, b) NLOS distance.

Fig. 11 presents the diffraction loss samples calculated from the different measurements with respect to both interaction angle and NLOS distance for the different polarization configurations. In the figure, it is possible to see that both polarizations present a similar behavior. It is important to remark that diffraction loss can be estimated by applying knife-edge formulation [17] over the geometry of the scenario by simply assuming that the corner of the building acts as a knife-edge, as illustrated in Fig. 6.c. By assuming a maximum reflection loss of approximately 20 dB, as it was found in Section III.B, it can be concluded that reflection becomes already dominant for diffraction interaction angles larger than 5 degrees and NLOS distances over approximately 1 m inside the street canyon.

D. Transmission (Penetration Loss)

Finally, the outdoor-to-indoor propagation was addressed. Measurements were performed at three different locations at the back-side part of the building, considering different facade elements as shown in Fig. 12: a) Modern window: 2-layered energy-efficient glass window with metal frame, b) Modern door: 3-layered energy-efficient glass panels with metal frames, c) Modern wall: 45 cm thick multi-layer wall composed, of reinforced-concrete (mainly) and brick.

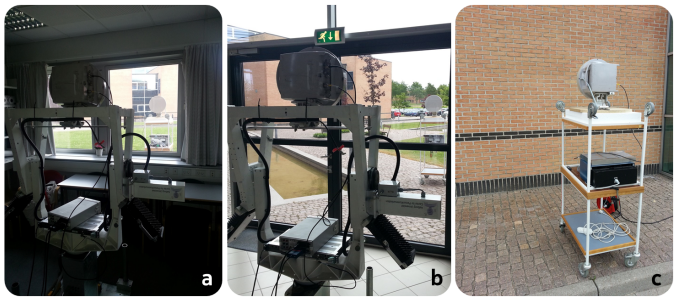

Fig. 12. Detailed overview of the facade elements considered for penetration loss characterization: a) modern window, b) modern door, c) modern wall.

TABLE I
MEASURED ATTENUATION AT 38 GHZ FOR THE DIFFERENT FACADE ELEMENTS AND POLARIZATION CONFIGURATIONS

Polarization	Modern window	Modern door	Concrete wall
VV	25 dB	40 dB	
HH	N/A	37 dB	$>$ 91 dB
VH	22 dB	35 dB	

Attenuation (penetration loss) was computed following a similar procedure to our previous study [11], in order to characterize the transmission propagation mechanism in this particular scenario. Penetration loss (L_p) is defined in (10) as the difference between a reference LOS measurement at a distance equal to a total path between TX and RX ($d_{out}+d_{in}$) and the outdoor-to-indoor measurement ($P_{rx,p}$), based on the geometry presented in Fig. 6.d.

$$L_p[\text{dB}] = P_{rx,LOS}(d_{out}+d_{in}) - P_{rx,p}(d_{out}+d_{in}) \quad (10)$$

Practically, this set of measurements, performed with normal incidence, should serve as a lower bound on the expected penetration loss in real scenarios, where different incident/grazing angles will cause to experience higher attenuation [11, 18]. Table I summarizes the attenuation values measured for the different elements and polarizations. As it can be seen, small polarization effects are observed and the values are quite similar polarization-wise. On average, the modern window presents an attenuation of 23.5 dB, while the modern door presents an attenuation of 37.3 dB. This higher value for the door can be explained due to the extra layer of IRR (infra-red rejection) metal-coated glass. In the case of the modern wall, no signal was detected throughout the measurement, which indicates an attenuation higher than 91 dB based on the maximum measurement equipment dynamics at the minimum TX-RX distance considered ($d_{out} = d_{in} = 1.8$ m).

The study is completed with Fig. 13, where the frequency-dependency of the attenuation is analyzed for the different elements, by combining the measurements presented in this paper for 38 GHz with the ones reported in our previous work for the frequency range from 800 MHz to 18 GHz [11].

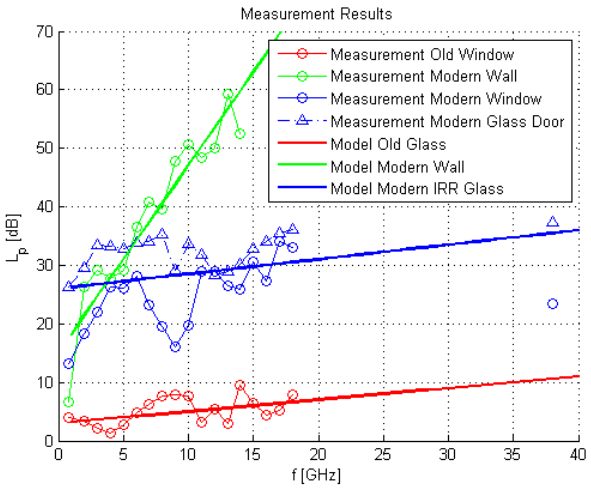

Fig. 13. Measured attenuation and frequency-dependent models for different facade elements.

TABLE II
FREQUENCY-DEPENDENT PENETRATION LOSS MODELS

Element	Model
Modern Wall	$L_p[\text{dB}] = 3.2 \cdot f + 15$
Modern IRR Glass	$L_p[\text{dB}] = 0.25 \cdot f + 26$
Old Glass	$L_p[\text{dB}] = 0.2 \cdot f + 3$

Based on the entire set of available data across frequencies, simple single-slope models for frequency-dependent penetration loss are provided in Table II. According to the model, the attenuation predicted for the modern wall at 38 GHz would be 136.6 dB, which is in line with the previous observations derived from the measurements. The model for modern IRR glass considers all together the data from the modern window and modern door. As it can be seen, the set of measurements at 38 GHz follows the trends observed in the lower frequency bands: the modern door presents an attenuation a bit above the model, while the modern window seems to keep the irregular behavior with frequency that leads to the "low" attenuation at 38 GHz. As a reference, this model is in good agreement with the data and observations reported in [19]. Finally, a model for old glass (single-layered) is also provided based on our previous data. It can be used as a reference for comparison between old and modern building constructions, and confirms the big impact of the different materials on radio propagation, as it was already pointed out in our previous study. According to this model, a single layered window with no metal coating would present a low attenuation of 10.6 dB at 38 GHz.

IV. Conclusions and Future Work

This paper presented a measurement-based study of 38 GHz mm-wave propagation in urban scenarios. The analysis focused on the characterization of the different radio propagation phenomena through a set of controlled measurements performed with ultra narrow-beam antennas located close to street level. The results are useful for development of ray-based channel models, as well as for calibration of existing ray-tracing tools. From the investigation it is concluded that, at 38 GHz, propagation in urban outdoor scenarios is driven mainly by line-of-sight propagation and reflection, although, as demonstrated, scattering and diffraction are also present. The measurement results verify that, in line-of-sight conditions, propagation follows free space. A set of empirical models was provided for characterization of reflection and scattering losses, as well as for outdoor-to-indoor penetration loss. In the scenario considered, a maximum reflection loss of approximately 20 dB was found for normal incidence over a modern building. Scattered components were shown to be spread with some strength up to 30 degrees around the main reflected component. Diffraction loss was found to be very strong, and predictable by using simple knife-edge calculations. The different measurements in NLOS conditions, confirmed how reflection becomes dominant over diffraction for interaction angles larger than 5 degrees, which in typical urban scenarios is translated into a distance of just a few meters inside street canyons. Penetration loss was found to range from 23.5 to 37.5 dB for a modern building composed of metal-coated isolation materials. Polarization issues were also addressed, finding a very similar behavior for both vertical and horizontal polarizations.

As future work, an extension of the study to different cm-wave and mm-wave frequency bands will be considered.

Acknowledgment

The authors would like to express their gratitude to Kristian Bank, Assistant Engineer from the Department of Electronics Systems, Aalborg University, for his effort and support with the measurement setup.

References

[1] P. Mogensen *et al.*, "5G Small Cell Optimized Radio Design", *IEEE Global Communications Conference (GLOBECOM) Workshops*, pp. 111-116, 9-13 December 2013.

[2] T. S. Rappaport *et al.*, "Millimeter Wave Mobile Communications for 5G Cellular: It Will Work!", *IEEE Access*, vol. 1, pp. 335-349, May 2013.

[3] Nokia Networks, "5G Ultra-Wideband Enhanced Local Area Systems at Millimeter Wave", [Online], September 2013.

[4] Y. Shen *et al.*, "Millimeter Wave Line-of-Sight Digital Radio at 38 GHz", *Asia-Pacific Microwave Conference (APMC)*, vol.1, pp. 21-24, 2-5 December 1997.

[5] S. Dynes, and T. Gordon, "38 GHz Fixed Links in Telecommunications Networks", *IEE Colloquium on Exploiting the Millimetric Wavebands*, pp. 5/1-5/4, 7 January 1994.

[6] P. B. Papazian *et al.*, "Initial Study of the Local Multipoint Distribution System Radio Channel", NTIA Report 94-315, August 1994.

[7] H. Xu *et al.*, "Measurements and Models for 38-GHz Point-to-Multipoint Radiowave Propagation", *IEEE Journal on Selected Areas in Communications*, vol. 18, no. 3, pp. 310-321, March 2000.

[8] J. N. Murdock *et al.*, "A 38 GHz Cellular Outage Study for an Urban Outdoor Campus Environment", *IEEE Wireless Communications and Networking Conference (WCNC)*, pp. 3085-3090, 1-4 April 2012.

[9] A. I. Sulyman *et al.*, "Radio Propagation Path Loss Models for 5G Cellular Networks in the 28 GHz and 38 GHz Millimeter-Wave Band", *IEEE Communications Magazine*, vol. 52, no. 9, pp. 78-86, September 2014.

[10] T. S. Rappaport *et al.*, "38 GHz and 60 GHz Angle-dependent Propagation for Cellular & Peer-to-Peer Wireless Communications", *IEEE International Conference on Communications (ICC)*, pp. 4568-4573, 10-15 June 2012.

[11] I. Rodriguez *et al.*, "Radio Propagation into Modern Buildings: Attenuation Measurements in the Range from 800 MHz to 18 GHz", *IEEE Vehicular Technology Conference (VTC-Fall)*, pp. 1-5, 14-17 September 2014.

[12] I. Rodriguez *et al.*, "Path Loss Validation for Urban Micro Cell Scenarios at 3.5 GHz Compared to 1.9 GHz", *IEEE Global Communications Conference (GLOBECOM)*, pp. 3942-3947, 9-13 December 2013.

[13] C. A. Balanis, "Advanced Engineering Electromagnetics", Wiley, 1989.

[14] Rec. ITU-R P.1238-2, "Propagation Data and Prediction Methods for the Planning of Indoor Radiocommunication Systems and Radio Local Area Networks in the Frequency Range 900 MHz to 100 GHz", August 2001.

[15] O. Landron *et al.*, "A Comparison of Theoretical and Empirical Reflection Coefficients for Typical Exterior Wall Surfaces in a Mobile Radio Environment", *IEEE Transactions on Antennas and Propagation*, vol. 44, no. 3, pp. 341-351, March 1996.

[16] A. Seville *et al.*, "Building Scatter and Vegetation Attenuation Measurements at 38 GHz", *International Conference on Antennas and Propagation*, vol. 2, pp. 46-50, 4-7 April 1995.

[17] W. C. Y. Lee, "Mobile Communications Engineering", 2nd Edition, McGraw Hill, 1983.

[18] J. E. Berg, "Building Penetration Loss Along Urban Street Microcells", *IEEE International Symposium on Personal, Indoor and Mobile Radio Communications*, vol. 3, pp. 795-797, 15-18 October 1996.

[19] H. Zhao *et al.*, "28 GHz Millimeter Wave Cellular Communication Measurements for Reflection and Penetration Loss in and around Buildings in New York City", *IEEE International Conference on Communications (ICC)*, pp. 5163-5167, 9-13 June 2013.